Long-term Hydrometeorological Time-series Analysis over the Central Highland of West Papua

Sandy H. S. Herho [a,b,1,*], Dasapta E. Irawan [c], Rubiyanto Kapid [d], Siti N. Kaban [e]

[a] Department of Earth and Planetary Sciences, University of California, Riverside, USA

[b] Department of Geology, university of Maryland, College Park, USA

[c] Applied Geology Research Group, Bandung Institute of Technology (ITB), Bandung, Indonesia

[d] Paleontology and Quaternary Geology Research Group, Bandung Institute of Technology (ITB), Bandung, Indonesia

[e] School of Architecture, Planning and Preservation, University of Maryland, College Park, MD, USA

[1] sandy.herho@email.ucr.edu

* corresponding author

ARTICLE INFO

ABSTRACT

This article presents an innovative data-driven approach for examining long-term temporal rainfall patterns in the central highlands of West Papua, Indonesia. We utilized wavelet transforms to identify signs of a negative temporal correlation between the El Niño-Southern Oscillation (ENSO) and the 12-month Standardized Precipitation Index (SPI-12). Based on this cause-and-effect relationship, we employed dynamic causality modeling using the Nonlinear Autoregressive with Exogenous input (NARX) model to predict SPI-12. The Multivariate ENSO Index (MEI) was used as an attribute variable in this predictive framework. Consequently, this dynamic neural network model effectively captured common patterns within the SPI-12 time series. The implications of this study are significant for advancing data-driven precipitation models in regions characterized by intricate topography within the Indonesian Maritime Continent (IMC).

1. Introduction

The central highlands of West Papua are an integral part of the province of Papua, which is the easternmost province of Indonesia (Fig. 1). The region has a complex landscape, with rugged and hilly terrain. Notably, some of Indonesia's highest peaks, including Carstensz Pyramid (5030 m.a.s.l.), Trikora Peak (4730 m.a.s.l.), Yamin Peak (4595 m.a.s.l.), and Mandala Peak (4700 m.a.s.l.), are located within the central highlands of West Papua. The intricate geomorphological features of the area are a manifestation of the geological and tectonic processes that have shaped its topography.

According to [31], the formation of the Papua Island emerged from the subduction process between the Australian Plate and the Pacific Plate. This convergent process and the resultant deformation of these plates commenced in the Eocene era and have persisted up to the present day [7]. The Australian Plate, lying beneath the Arafura Sea and extending northward, forms the foundation of the southern segment of the central highlands of West Papua. This foundation comprises sedimentary rocks of various ages, ranging from Palaeozoic to Mid-Quaternary [11].

Stretching from the equator to 12°S, the central highlands of West Papua qualify as a tropical region largely influenced by the monsoonal asymmetric cycle, akin to the prevailing conditions across much of the Indonesian Maritime Continent (IMC) ([32], [28], [6], [40]). In tandem with these monsoonal

influences, the area is subject to localized effects, including mountain deflection and local warming, which exert control over rainfall patterns [4]. Additionally, the El Niño-Southern Oscillation (ENSO) phenomenon leaves its imprint on the seasonal rainfall dynamics in Papua; El Niño events, for instance, can lead to reduced rainfall in the region [29].

The central highlands of West Papua experience varying precipitation levels ranging from 2500 to 4500 mm/year. The number of rainy days varies from 148 to 175 per year, while average surface air temperatures fluctuate between 29°C and 31.8°C. Relative humidity in the area ranges between 79% and 81%. Consequently, the central highlands of Papua emerge as one of the most moisture-laden regions within the IMC [26].
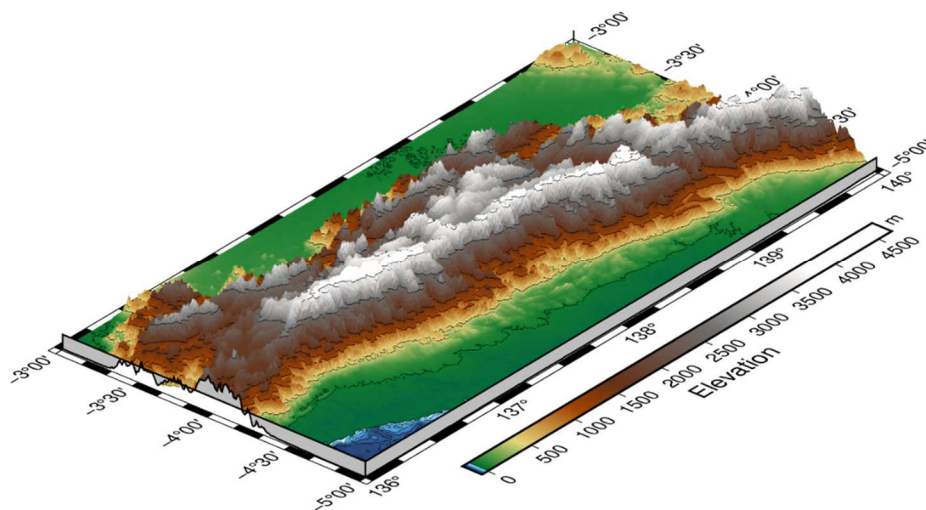
Figure 1. Digital Elevation Model (DEM) of the central highlands of West Papua (rendered using PyGMT [37])

Studies investigating the rainfall characteristics of the Papua region are scarce, making it difficult for researchers to access relevant information. This scarcity may be due to the intricate topography prevalent in the area, which makes conventional numerical approaches challenging to investigate (e. g. [14], [8], [24], [9]). Additionally, the limitations imposed by the aerial distribution of rain gauges and radar networks, under the purview of the Indonesian Agency for Meteorology, Climatology and Geophysics (BMKG), could contribute to this shortage [39].

To address this issue, we propose a data-driven approach [30]. By leveraging ERA5 monthly averaged data at single levels [20], we aim to uncover the attributes and predictability of long-term precipitation time series across the central highlands of Papua. This approach offers an alternative means of examining and understanding the nuanced aspects of rainfall behaviour in the region, circumventing the challenges posed by complex terrain and sparse meteorological instrumentation.

2. Materials and Methods

2.1 Long-term Drought / Pluvial Time-series Reconstruction

This subsection focuses on reconstructing long-term meteorological droughts and pluvial events in the central highlands of West Papua. To quantitatively assess these occurrences, we used the SPI-12 index [27], [17]). This index is a well-established metric for evaluating extended meteorological droughts and pluvial periods. Its effectiveness in reconstructing droughts spanning the past millennium within the Indonesian Maritime Continent (IMC) has been documented [19].

Our initial step entailed computing the spatial average of terrestrial precipitation across the central high lands of West Papua, utilizing the ERA5 monthly averaged data on single levels [20]. Mathematically defined in equation (1), the spatial average for a precipitation field $p(\phi, \theta, t)$ on a spherical surface [34] is expressed as:

$$\bar{p}(t) = \frac{1}{4\pi} \iint p(\phi, \theta, t) \, cos(\phi) d\phi d\theta \tag{1}$$

Where ϕ is latitude, θ is longitude, and t is time. To handle the gridded dataset, a discretized form of equation (1) was needed. The discrete form of equation (1) for a grid resolution $\Delta\phi \times \Delta\theta$ is defined in equation (2):

$$\bar{p}(t) = \sum_{i,j} p(i,j,t) \frac{cos(\phi_{i,j})\Delta\phi\Delta\theta}{4\pi} \tag{2}$$

Where i, j are coordinate indices for each the grid box of precipitation data over the central highlands of West Papua, and ϕ and θ are in radian. Since ERA5 precipitation data has a spatial resolution of $0.25° \times 0.25°$, then $\Delta\phi = \Delta\theta = (0.25/180)\pi = \pi/720$. By substituting this information into equation (2), the following equation was obtained:

$$\bar{p}(t) = \sum_{i,j} p(i,j,t) \frac{cos(\phi_{i,j})(1/720)^2}{4} \tag{3}$$

We solved the calculation in the equation (3) using the built-in function in the xarray library [22] in the Python computational environment.

The spatial average of monthly precipitation was used to calculate SPI-12. SPI-12 involves comparing the rainfall over 12 consecutive months with the corresponding 12 months from preceding years. This temporal scale provides insights into long-term rainfall patterns ([27], [17]). The SPI at this scale represents the cumulative effect of prior periods that could have been either above or below the normal range. Correlations can be observed between SPI-12 and stream flows, reservoir conditions, and even groundwater levels. In several countries, SPI-12 has exhibited the closest correlation with the Palmer Drought Severity Index (PDSI), leading some to suggest that both indices reflect the same conditions [16].

SPI was calculated using statistical methods as follows:

$$G(x) = \int_0^x g(x, \hat{\alpha}, \hat{\beta})dx = \frac{1}{\hat{\beta}^{\hat{\alpha}}\Gamma(\hat{\alpha})} \int_0^x x^{\hat{\alpha}-1} e^{-x/\hat{\beta}} \tag{4}$$

Where α is a shape parameter, β is a scale parameter, $\Gamma(\alpha)$ is a gamma function, and x is precipitation values. Equation (4) applies if $x > 0$ (otherwise $g(x, \hat{\alpha}, \hat{\beta}) = 0$, which in this case applied to precipitation data which are always within the range $(0, +\infty)$. In order to match the gamma distribution with precipitation data, it was necessary to estimate the α and β parameters using the maximum likelihood approximation which is defined as follows:

$$\hat{\alpha} = \frac{1}{4A}\left(1 + \sqrt{\frac{4A}{3}}\right) \tag{5}$$

$$\hat{\beta} = \frac{\bar{x}}{\hat{\alpha}} \tag{6}$$

Where A is defined by equation (7),

$$A = ln(\bar{x}) - \frac{\sum ln(x)}{n} \tag{7}$$

Where n is the number of observations. For $\hat{\alpha} > 0$, $\Gamma(\hat{\alpha})$ is defined by equation (8),

$$\Gamma(\hat{\alpha}) = \int_0^{+\infty} x^{\hat{\alpha}-1} e^{-x} \, dx \tag{8}$$

The gamma distribution is undefined for $x = 0$ and $q = P(x = 0) > 0$, where q is the probability of zero percipitation. Therefore, the cumulative probability distribution is defined by equation (9):

$$H(x) = q + (1 - q)G(x) \tag{9}$$

The gamma distribution $G(x)$ was then converted to be a normal standard with zero mean and standard deviation of one, so that the SPI index Z was obtained using equation (10):

$$Z = \begin{cases} -t - \dfrac{c_0 + c_1 t + c_2 t^2}{1 + d_1 t + d_2 t^2 + d_3 t^3} \ , & for\ 0 < H(x) \le 0.5 \\ t - \dfrac{c_0 + c_1 t + c_2 t^2}{1 + d_1 t + d_2 t^2 + d_3 t^3} \ , & for\ 0.5 < H(x) < 1 \end{cases} \tag{10}$$

Where t is defined by equation (11):

$$t = \begin{cases} \sqrt{ln\left(\dfrac{1}{(H(x))^2}\right)} \ , & for\ 0 < H(x) \le 0.5 \\ \sqrt{ln\left(\dfrac{1}{(1 - H(x))^2}\right)} \ , & for\ 0.5 < H(x) < 1 \end{cases} \tag{11}$$

And the constants are defined as follows:

$$\begin{cases} c_0 = 2.516, \\ c_1 = 0.803, \\ c_2 = 0.01, \\ d_1 = 1.433, \\ d_2 = 0.109, \\ d_3 = 0.001. \end{cases} \tag{12}$$

In order to simplify the calculation process, we used the SPEI package [3] in the R computational environment.

2.2 Identifying ENSO-driven Pattern in SPI-12

The influence of the ENSO signal within the IMC ([29], [39], [41]) is an important aspect that must be considered when analyzing drought and pluvial events in the central highlands of West Papua. This subsection provides a comprehensive examination of the temporal effects of ENSO on SPI-12, using the Multivariate ENSO Index (MEI) [38]. To assess the impact of ENSO on drought and pluvial occurrences in the study area over time, we utilized wavelet transforms, a prevalent algorithm for analyzing geophysical signal patterns. Wavelet transforms have an advantage over other power spectrum methods as they can capture non-linear signals within time series data by utilizing discrete wave packets (wavelets) with inherently smooth terminations, instead of the conventional use of sine and cosine wave functions [25].

In this study we used an extension of the Morlet wavelet (ψ) [36] to model ENSO and SPI-12 signals, which is defined by:

$$\psi(t) = e^{-\frac{1}{4}} e^{-iw_0 t} e^{-\frac{1}{2}t^2} \ , t = 1,2,3, \dots \tag{13}$$

Where t is the position where the wavelet operates in a time series with a narrow range of observations.

In general, wavelets have two main components, namely time or position k and frequency f. The k parameter has an important role in detecting the exact location of a wavelet by relocating the wavelet over a period of time, while f is useful for monitoring the convex wavelet to localize different frequencies. By transforming $\psi,$, we got the $\psi_{k,f}$ parameter as follows:

$$\psi_{k,f}(t) = \frac{1}{\sqrt{h}} \psi\left(\frac{t-k}{f}\right), k, f \in R, \ f \neq 0 \tag{14}$$

Equation (15) describes the modeling of a time series $x(t)$ into a wavelet transform,

$$W_x(k,f) = \int_{-\infty}^{+\infty} x(t) \frac{1}{\sqrt{f}} \psi\left(\frac{t-k}{f}\right) dt \tag{15}$$

The signal power in the time series $x(t)$ itself was measured using the wavelet power spectrum $WPSx(k,f)$ which is defined as follows:

$$WPS_x(k,f) = |W_x(k,f)|^2 \tag{16}$$

In order to simplify the process of calculating the continuous wavelet power spectrum on ENSO and SPI-12 data, we used the PyCWT library [23] in the Python computational environment.

To measure the relationship between the two quantitatively, we needed another mathematical tool, namely the wavelet coherence (WTC). We used WTC to find time-frequency-based causality between two time-series data, in this context MEI. $x(t)$ and SPI-12 $y(t)$. The first step we take was to find the cross-wavelet transforms (XWT) of the two time-series data (equation (17)):

$$W_{xy}(k,f) = W_x(k,f) \overline{W_y(k,f)} \tag{17}$$

Where $W_{xy}(k,f)$ is the XWT of the two time-series data. Then to find WTC value, the equation (18) was used as follows:

$$R^2(k,f) = \frac{\left|C(f^{-1} W_{xy}(k,f))\right|^2}{C(f^{-1}|W_x(k,f)|^2) \, C\left(f^{-1}|W_y(k,f)|^2\right)} \tag{18}$$

C parameter shows the time and smoothing process over the duration of time in within the range of $0 \leq R^2(k,f) \leq 1$. When $R^2(k,f)$ approaches one, a strong correlation can be expected between MEI and SPI-12. Conversely, if $R^2(k,f)$ is zero, then there is no correlation between the two variables. To find out the positive or negative correlation of the two time-series data, we use the phase difference equation (equation (19)) as follows:

$$\phi_{xy}(k,f) = arctan\left(\frac{\Im\{C(f^{-1}W_{xy}(k,f))\}}{\Re\{C(f^{-1}W_{xy}(k,f))\}}\right) \tag{19}$$

Where $\Re$ shows the real part and $\Im$ shows the imaginary part. To simplify the WTC calculation process, we used the open-source MATLAB® Toolbox by [15].

2.3 ENSO - SPI-12 Dynamic and Predictability

To ensure accurate SPI-12 predictions, we used the Nonlinear Autoregressive with Exogenous input neural networks (NARX) model. This model was effective in capturing the dynamic relationship between ENSO and long-term drought/pluvial events in the central highlands of West Papua. NARX, a type of recurrent dynamic neural network, is commonly used to model non-linear associations within attributes across time series data ([10], [2], [5]). Fig. 2 provides a schematic representation of the simplified NARX structure. Input data was introduced into delayed units, which served as memory repositories for previous inputs. Outputs derived from the NARX model were also stored within delayed units and then directed into hidden units for further processing.

NARX model is defined as a nonlinear mapping function f [10] as follows:

$$y_t = f\left(y_{t-1}, y_{t-2}, \ldots, y_{t-d_y}, x_{t-1}, x_{t-2}, \ldots, x_{t-d_x}\right) \tag{20}$$

Where y is a target (SPI-12) and x are attributes (MEI); and $dx \geq 1, dy \geq 1, dy \geq dx$ are delays. The nonlinear f function itself is generally unknown, and must be approximated using the existing data. There are various ways to approximate this function, in this study we use multilayer perceptrons provided by PyNeurGen library [35] in the Python computational environment. We used 1-time steps of delay for each of the input (x) and output (y) attributes. In addition, we also split incoming weights, 60% for MEI and 30% for SPI-12. We made use of the following sigmoid function for activation of the perceptrons:

$$S(x) = \frac{1}{1+e^{-x}} \tag{21}$$

We divided SPI-12 into two parts, 85% for the training set and 15% (January 1980 - December 2014) for the testing set (January 2015 - December 2020). We used a moderate steps of learning rate of 35% for the optimization process using the Stochastic Gradient Descent (SGD) algorithm. Our NARX model was run for 10 epochs without activating the random testing parameter to maintain the order of time-series data. To evaluate the model performance, we used the Mean Squared Error (MSE) which is shown by equation (22) below:

$$MSE = \frac{1}{n}\sum_{i=1}^{n}(\hat{y}_i - y_i)^2 \tag{22}$$

Which is the sum series of the squared differences of the observed target y_i and predicted values $\hat{y}_i$, which was then divided by the total number of test samples n.
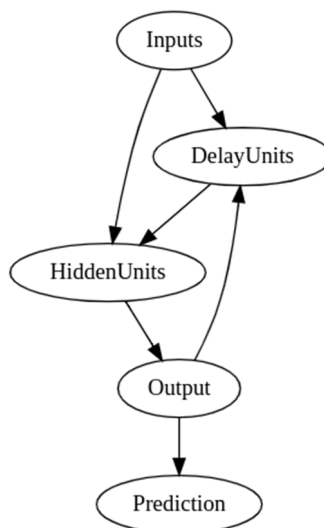

Figure 2. Simple schematic diagram of NARX model

3.   Results and Discussion

The calculation result of Equation (3) is the spatial average of monthly precipitation time-series shown in Fig. 3. Fig.3 shows that rainfall events occurred in each month of the study period. To examine the pattern of monthly rainfall, we averaged the data for each month, as shown in Fig. 4. It can be observed from Fig. 4 that the monthly rainfall pattern in the central highlands of West Papua has one peak and one trough, which corresponds to the rainfall pattern in Region A [1], but with a shift in the onset of wet and dry seasons due to other local factors. The seasonal rainfall patterns over the central highlands of West Papua (Fig. 4) exhibit an asymmetric pattern between boreal summer and winter, and between boreal spring and fall.
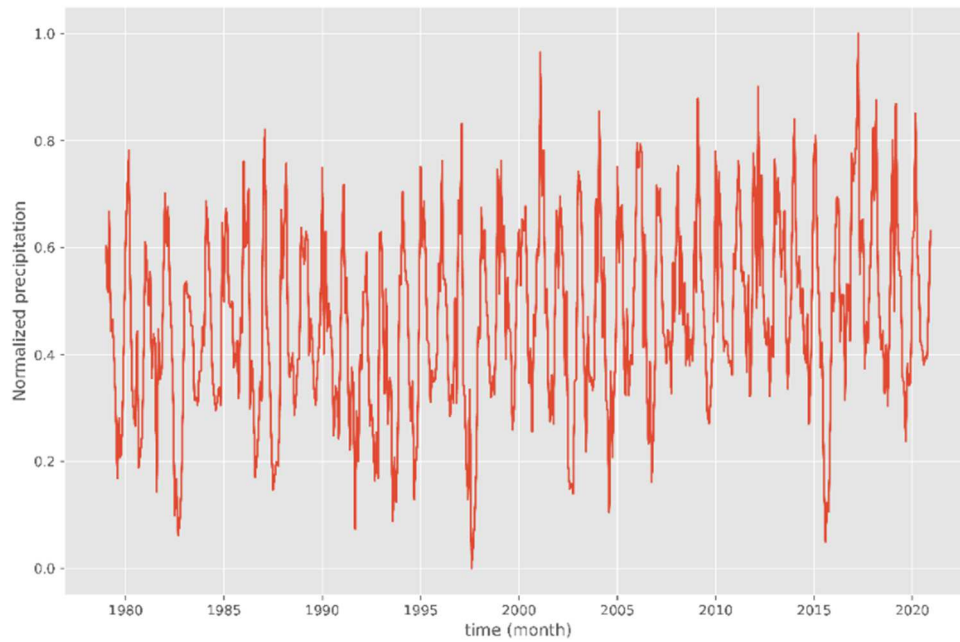
Figure 3. Variations in the normalized monthly precipitation data from ERA5 over the central highlands of West Papua from January 1979 to December 2020
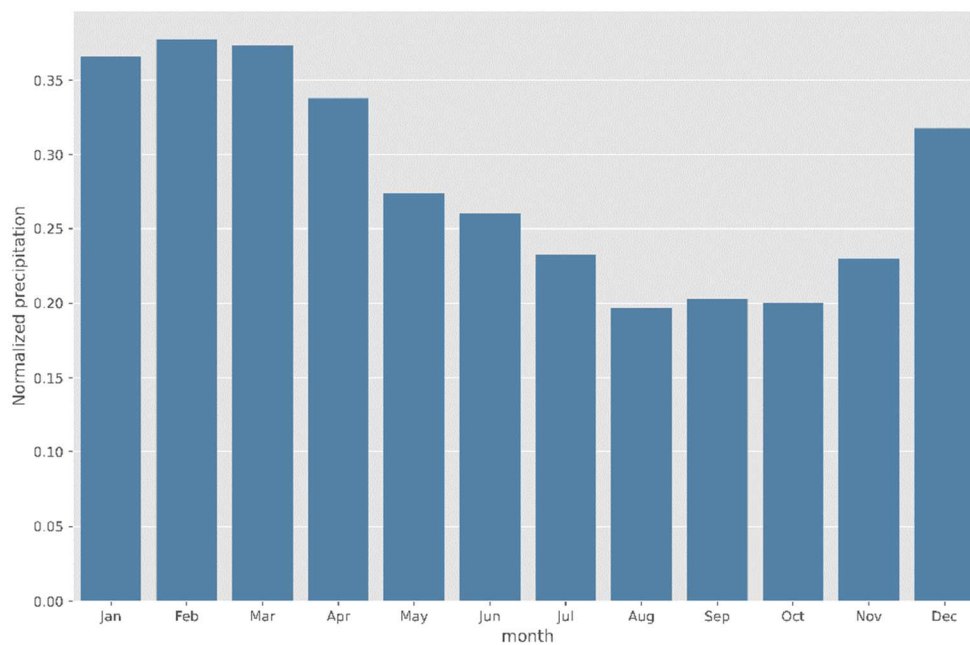

Figure 4. Normalized average monthly precipitation over the central highlands of Papua

Fig. 5 shows the result of the SPI-12 reconstruction from January 1980 to December 2020. There are similarities between WPS and ENSO (Fig. 6) as well as SPI-12 (Fig. 7). To

establish the relationship between SPI-12 and MEI more rigorously, a meticulous WTC computation was undertaken. The results of this WTC calculation are elegantly presented in Fig. 8, providing a graphical illustration that effectively encapsulates the derived results.
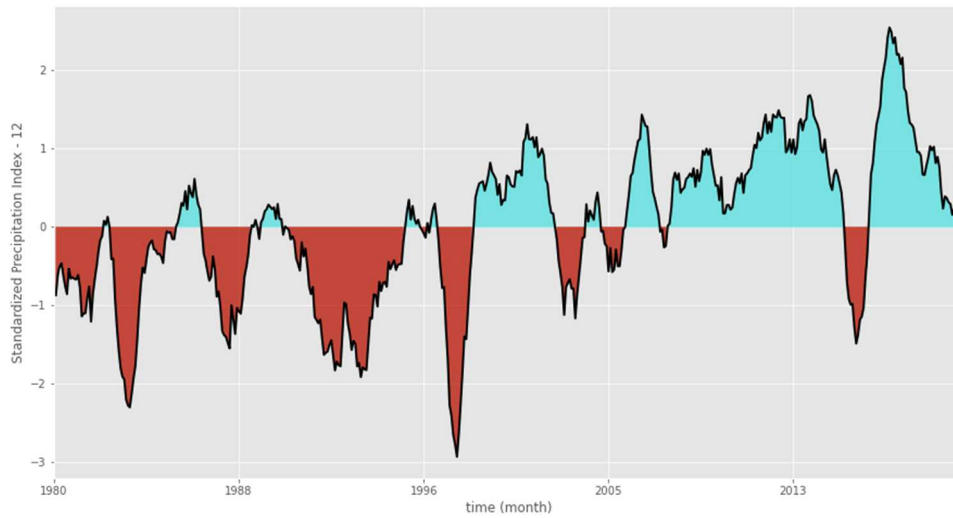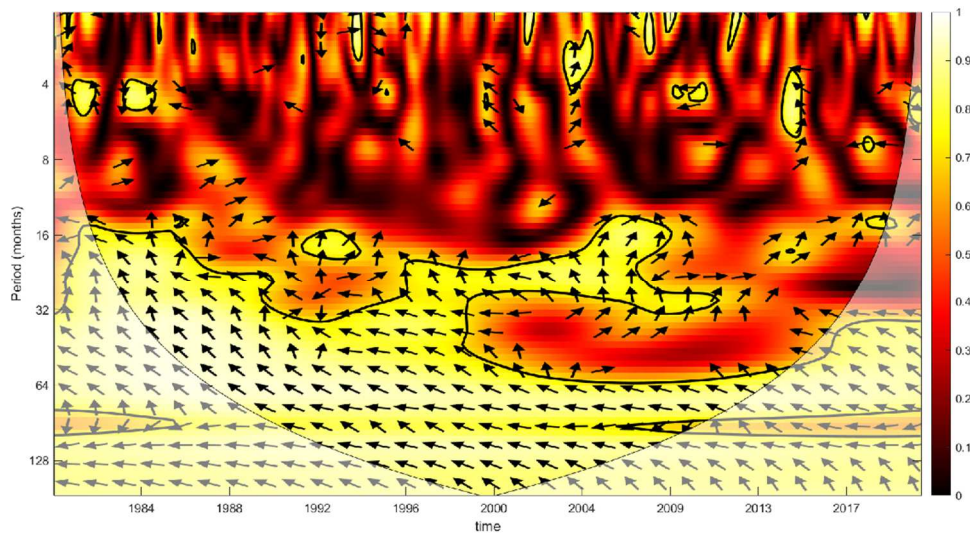

Figure 5. SPI values over the central highlands of West Papua from January 1980 to December 2020 with a 12-month time scale. Negative SPI-12 describes dry conditions (red), whereas positive SPI-12 describes wet conditions (blue).
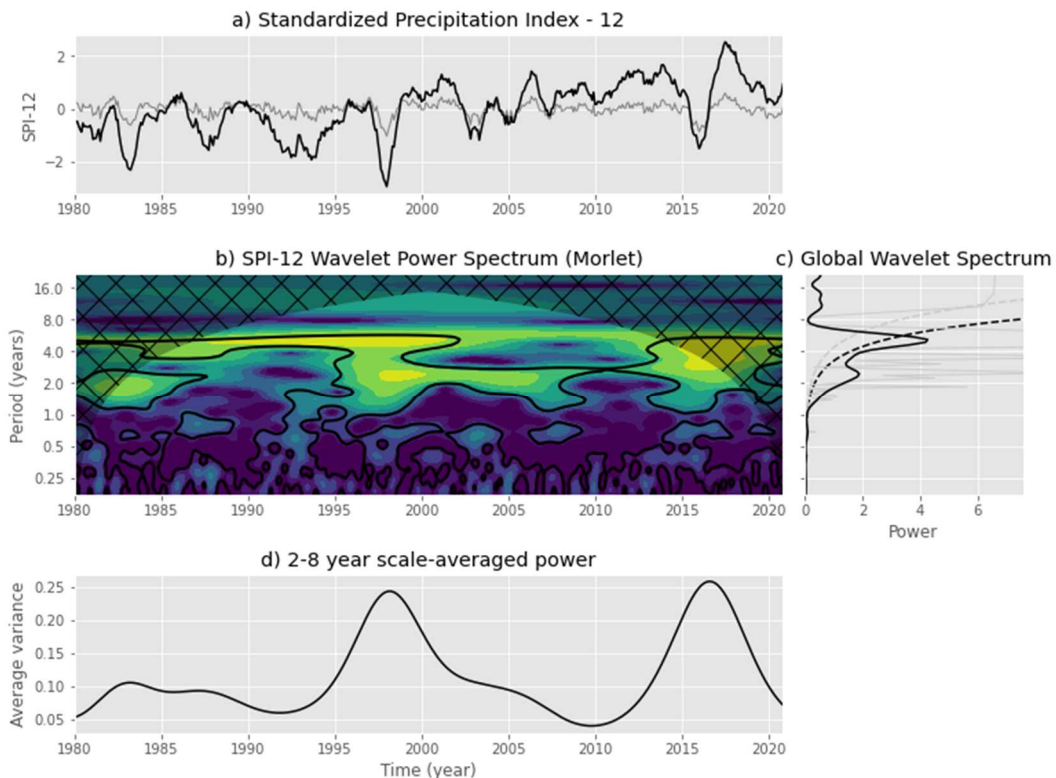
Figure 6. Continuous wavelets transform for the SPI-12. These plots clearly show significant periodicity at 2 - 8-year cycle.
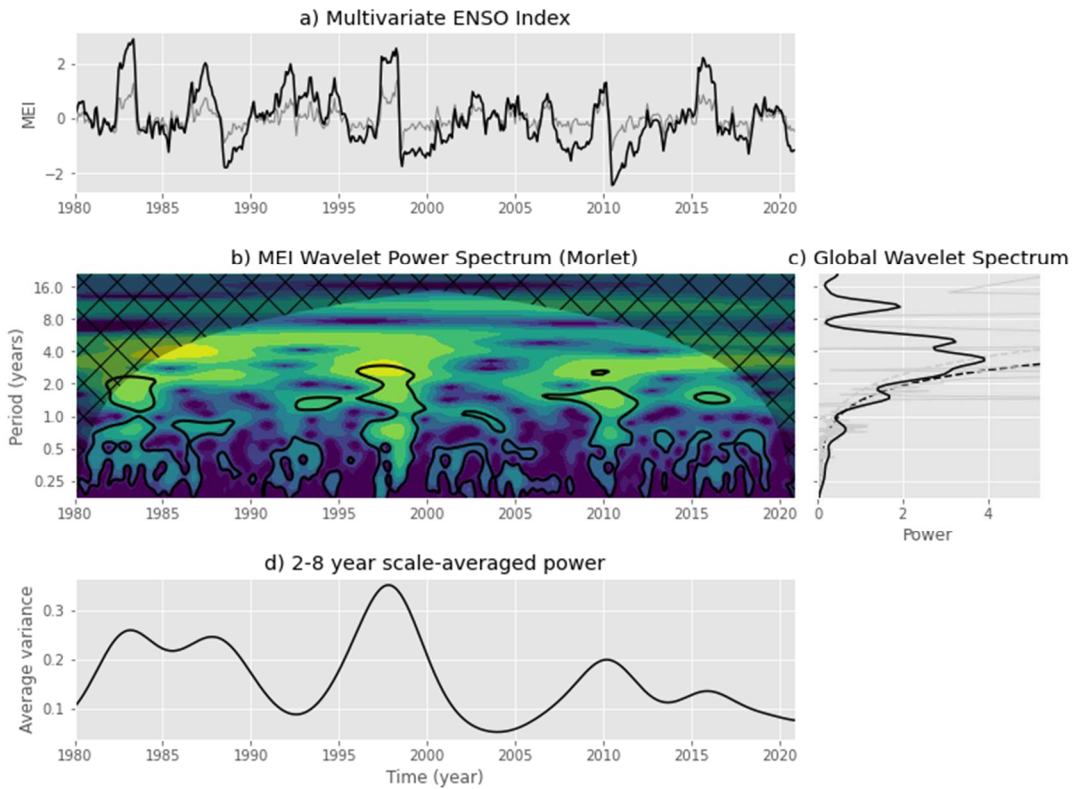
Figure 7. Continuous wavelets transform for the MEI. These plots clearly show significant periodicity at 2 -8-year cycle.


Figure 8. Wavelet coherence between MEI and SPI-12. The colour scale on the right side of the figure represents the level of correlation between ENSO and long-term meteorological drought/pluvial events over the central highlands of West Papua. The light-yellow colour indicates high correlations among the variables, while the thick black contour designates the 5% significance level against red noise and the cone of influence (COI) where edge effects might distort the picture is shown as a lighter shade. The arrows show the phasing direction (right: in-phase, left: anti-phase, down: MEI leading SPI-12 by $\pi/2$, up: SPI-12 leading MEI by $\pi/2$).

As seen in Fig. 8, WTC can capture the inversely proportional relationship between MEI and SPI-12 at 32-to-128-month periodicity. This causal effect reveals that precipitation over the central highlands of West Papua increases during La Niña and decreases during El Niño.

The MSE of NARX model at each training epoch can be seen in Fig. 9. It exhibits sharp decline at the first epoch and finally leveling out until the end of the last training epoch. The overall MSE evaluation result in the test set is 0.011. The comparison between the NARX model prediction results and the actual SPI-12 is shown in Fig. 10. Overall, the model tends to overestimate and underestimate certain extreme values, although it adequately captures the general pattern of SPI-12.
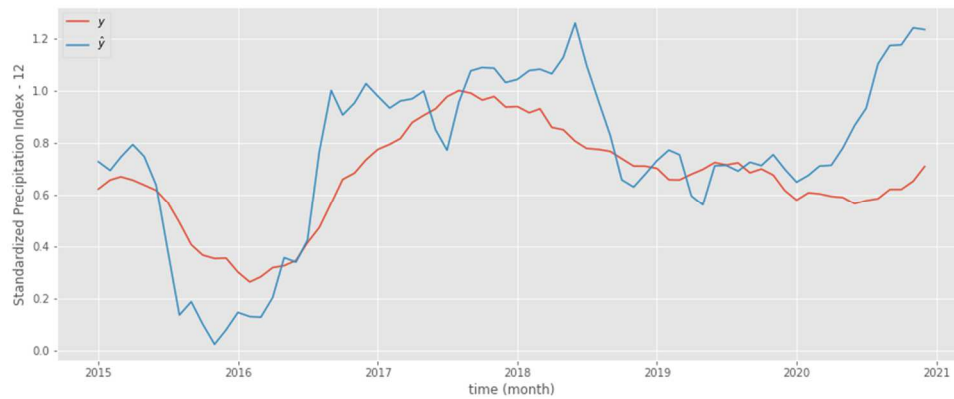
Figure 9. MSE by epoch for NARX model
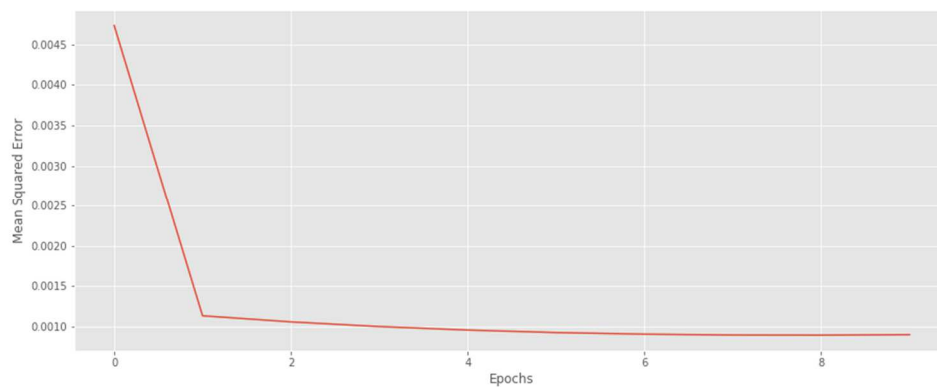
Figure 10. Actual y (red) and predicted ŷ (blue) SPI-12 values for NARX model

4.   Conclusion

Our research endeavors involved a thorough analysis of the SPI-12 time series dataset, which covers the central highlands of West Papua. Through a rigorous exploration, we aimed to unravel the complex relationships within this dataset, focusing specifically on the teleconnection pattern between ENSO and hydrometeorological drought/pluvial events in this region. We used wavelet transformations to investigate the underlying connections.

Our meticulous investigation led us to discover a discernible and noteworthy teleconnection pattern between ENSO and hydrometeorological drought/pluvial events in the central highlands of West Papua. We unraveled the complex web of relationships between these factors using wavelet transformations, revealing a finely woven tapestry of associations. Our analysis showed a significant and negative correlation between ENSO and the prevailing long-term rainfall patterns in this region. This finding is crucial in understanding the dynamics of climatic events in this area.

Using the patterns discerned from the wavelet coherence (WTC) analysis, we constructed a model that could encapsulate the nuanced temporal dynamics between ENSO and the intricate long-term rainfall patterns. We used the NARX algorithm, renowned for its efficacy in capturing complex non-

linear relationships. The NARX model enabled us to delve deeper into the interplay of climatic variables.

The predictions gleaned from the NARX model demonstrated its effectiveness in capturing the overarching trends embedded within the complex interdependence of ENSO and long-term rainfall patterns. The model's ability to encapsulate these trends augments our understanding of the underlying dynamics that govern these climatic phenomena. By distilling intricate data patterns into comprehensible insights, the NARX model emerges as a valuable asset in unraveling the complex tapestry of climatic interactions.

Our study's findings suggest potential avenues for further exploration and refinement. One avenue involves applying diverse, finely tuned optimization strategies to the NARX model, drawing inspiration from the work of [18]. Implementing early-stopping algorithms, as advocated by [12], is also significant to prevent overfitting during model training.

In addition to the NARX model, we need to conduct a comprehensive comparison involving a spectrum of robust sequence-to-sequence (seq2seq) machine learning algorithms. These include the Long-Short Term Memory (LSTM) [21], the Gated Recurrent Unit (GRU) [13], and the DeepAR model [33]. This evaluation aims to determine the optimal time-series model that faithfully encapsulates the intricate interplay of climatic variables in our dataset.

Our study also highlights the importance of comparing our findings with the outputs derived from Global Climate Models (GCMs). This comparative analysis can potentially illuminate the intricate physical processes underpinning the spatio-temporal dynamics connecting ENSO and long-term rainfall patterns across the central highlands of West Papua. In doing so, we can achieve a more holistic comprehension of the complex interactions that govern the climatic landscape of this region.

References

[1] Aldrian, E. and Susanto, R. D., 2003. Identification of three dominant rainfall regions within Indonesia and their relationship to sea surface temperature. International Journal of Climatology, 23(12), pp.1435–1452.

[2] Ang, M. R. C. O., Gonzalez, R. M. and Castro, P. P. M., 2014. Multiple data fusion for rainfall estimation using a NARX-based recurrent neural network – the development of the REIINN model. IOP Conference Series: Earth and Environmental Science, 17, p.012019.

[3] Beguería, S. and Vicente-Serrano, S., 2017. SPEI: Calculation of the Standardised Precipitation-Evapotranspiration Index. R package version 1.7.

[4] Boerema, J., 1938. Van Den Typen Regenval in Nederlandsch Indie (Rainfall types in Nederlands Indies). The Royal Observatory Magnetisch En Meteorologisch Batavia, Batavia.

[5] Caswell, J. M., 2014. A nonlinear autoregressive approach to statistical prediction of disturbance storm time geomagnetic fluctuations using solar data. Journal of Signal and Information Processing, 5, pp.42–53.

[6] Chang, C.-P., Wang, Z., McBride, J. and Liu, C.-H., 2005. Annual Cycle of Southeast Asia—Maritime Continent Rainfall and the Asymmetric Monsoon Transition. Journal of Climate, 18(2), pp.287 – 301.

[7] Charlton, T. R., 2000. Tertiary evolution of the Eastern Indonesia Collision Complex. Journal of Asian Earth Sciences, 18(5), pp.603–631.

[8] Chow, F. K., Schär, C., Ban, N., Lundquist, K. A., Schlemmer, L. and Shi, X., 2019. Crossing multiple gray zones in the transition from mesoscale to microscale simulation over complex terrain. Atmosphere, 10(5), p.274.

[9] Clifton, A., Barber, S., Stökl, A., Frank, H. and Karlsson, T., 2022. Research challenges and needs for the deployment of wind energy in hilly and mountainous regions. Wind Energy Science, 7(6), pp.2231–2254.

[10] Diaconescu, E., 2008. The use of narx neural networks to predict chaotic time series. World Scientific and Engineering Academy and Society (WSEAS), 3(3), pp.182–191.

[11] Dow, D. B. and Sukamto, R., 1984. Western Irian Jaya: The end-product of oblique plate convergence in the late tertiary. Tectonophysics, 106(1), pp.109–139.

[12] Gençay, R. and Qi, M., 2001. Pricing and hedging derivative securities with neural networks: Bayesian regularization, early stopping, and bagging. IEEE Transactions on Neural Networks, 12, pp.726 – 734.

[13]   Gers, F. A., Schmidhuber, J. and Cummins, F., 1999. Learning to forget: continual prediction with lstm. 1999 Ninth International Conference on Artificial Neural Networks ICANN 99. (Conf. Publ. No. 470), 2, pp.850–855.

[14]   Goger, B., Rotach, M. W., Gohm, A., Stiperski, I. and Fuhrer, O., 2016. Current challenges for numerical weather prediction in complex terrain: Topography representation and parameterizations. 2016 International Conference on High Performance Computing Simulation (HPCS), pp.890–894.

[15]   Grinsted, A., Moore, J. C. and Jevrejeva, S., 2004. Application of the cross wavelet transform and wavelet coherence to geophysical time series. Nonlinear Processes in Geophysics, 11(5/6), pp.561–566.

[16]   Guenang, G. M. and Kamga, F. M., 2014. Computation of the standardized precipitation index (spi) and its use to assess drought occurrences in cameroon over recent decades. Journal of Applied Meteorology and Climatology, 53(10), pp.2310 – 2324.

[17]   Guttman, N. B., 1999. Accepting the standardized precipitation index: A calculation algorithm1. Journal of the American Water Resources Association, 35(2), pp.311–322.

[18]   He, X., Zhao, K. and Chu, X., 2021. Automl: A survey of the state-of-the-art. Knowledge-Based Systems, 212, p.106622.

[19]   Herho, S., Syahputra, M. R. and Suwarman, R., 2018. A preliminary study of meteorological drought influences to social events over the maritime continent during the last millennium. Extended Abstract 98th American Meteorological Society Annual Meeting, 16th History Symposium, Austin, TX. American Meteorological Society.

[20]   Hersbach, H. et al., 2020. The ERA5 global reanalysis. Quarterly Journal of the Royal Meteorological Society, 146(730), pp.1999–2049.

[21]   Hochreiter, S. and Schmidhuber, J., 1997. Long Short-Term Memory. Neural Computation, 9(8), pp.1735–1780.

[22]   Hoyer, S. and Hamman, J., 2017. xarray: N-D labeled arrays and datasets in Python. Journal of Open Research Software, 5(1).

[23]   Krieger, S., Freij, N., Brazhe, A., Torrence, C. and Compo, G. P., 2017. PyCWT: spectral analysis using wavelets in Python. Python library version 0.3.0a22.

[24]   Largeron, C. et al., 2020. Toward snow cover estimation in mountainous areas using modern data assimilation methods: A review. Frontiers in Earth Science, 8, p.325.

[25]   Lau, K.-M. and Weng, H., 1995. Climate signal detection using wavelet transform: How to make a time series sing. Bulletin of the American Meteorological Society, 76(12), pp.2391 – 2402.

[26]   Marshall, A. and Beehler, B. M., 2007. The Ecology of Papua. Singapore: Periplus Editions (HK), vol. 1.

[27]   McKee, T. B., Doesken, N. J. and Kleist, J., 1993. The relationship of drought frequency and duration of the time scales. Proceeding 8th Conference on Applied Climatology, Anaheim, CA. American Meteorological Society.

[28]   Neale, R. and Slingo, J., 2003. The Maritime Continent and its role in the global climate: A GCM study. Journal of Climate, 16(5), pp.834–848.

[29]   Permana, D. S., Thompson, L. G. and Setyadi, G., 2016. Tropical West Pacific moisture dynamics and climate controls on rainfall isotopic ratios in southern Papua, Indonesia. Journal of Geophysical Research: Atmospheres, 121(5), pp.2222–2245.

[30]   Peters-Lidard, C. D. et al., 2017. Scaling, similarity, and the fourth paradigm for hydrology. Hydrology and Earth System Sciences, 21(7), pp.3701–3713.

[31]   Pigram, C. J. and Symonds, P. A., 1991. A review of the timing of the major tectonic events in the New Guinea Orogen. Journal of Southeast Asian Earth Sciences, 6(3), pp.307–318.

[32]   Ramage, C. S., 1968. Role of a tropical "maritime continent" in the atmospheric circulation. Monthly Weather Review, 96(6), pp.365 – 370.

[33]   Salinas, D., Flunkert, V., Gasthaus, J. and Januschowski, T., 2020. Deepar: Probabilistic forecasting with autoregressive recurrent networks. International Journal of Forecasting, 36(3), pp.1181–1191.

[34]   Shen, S. S. P. and Somerville, R. C. J., 2019. Climate Mathematics: Theory and Applications. Cambridge: Cambridge University Press.

[35]   Smiley, D., 2012. PyNeurGen: Python Neural Genetic Algorithm Hybrids. Python library version 0.3.1.

[36]   Torrence, C. and Compo, G. P., 1998. A practical guide to wavelet analysis. Bulletin of the American Meteorological Society, 79(1), pp.61 – 78.

[37]   Wessel, P. et al., 2019. The Generic Mapping Tools Version 6. Geochemistry, Geophysics, Geosystems, 20(11), pp.5556–5564.

[38]   Wolter, K. and Timlin, M. S., 2011. El niño/southern oscillation behaviour since 1871 as diagnosed in an extended multivariate enso index (mei.ext). International Journal of Climatology, 31(7), pp.1074–1087.

[39]   Yamanaka, M. D., 2016. Physical climatology of Indonesian maritime continent: An outline to comprehend observational studies. Atmospheric Research, 178-179, pp.231–259.

[40]   Yang, S., Zhang, T., Li, Z. and Dong, S., 2019. Climate variability over the Maritime Continent and its role in global climate variation: A review. Journal of Meteorological Research, 33(6), pp.993–1015.

[41]   Yoden, S., Otsuka, S., Trilaksono, N. J. and Hadi, T. W., 2017. Recent Progress in Research on the Maritime Continent Monsoon. In Chapter 6, pp.63–77.